Journal of Rock Mechanics and Geotechnical Engineering 8 (2016) 16–26

Contents lists available at ScienceDirect

Journal of Rock Mechanics and Geotechnical Engineering

journal homepage: www.rockgeotech.org

Full length article

The stress–strain–permeability behaviour of clay rock during damage and recompaction

Chun-Liang Zhang*

Gesellschaft für Anlagen- und Reaktorsicherheit (GRS) mbH, Braunschweig, 38122, Germany

ARTICLE INFO

Article history:
Received 6 August 2015
Received in revised form
13 October 2015
Accepted 23 October 2015
Available online 23 November 2015

Keywords:
Clay rock
Deformation
Damage
Compaction
Permeability

ABSTRACT

Characterisation and understanding of the stress–strain–permeability behaviour of a clay host rock during damage and recompaction are essential for prediction of excavation damaged zone and for assessment of its impact on the repository safety. This important issue has been experimentally studied in triaxial compression tests on the Callovo-Oxfordian clay rock in this study. The samples were sequentially loaded by (1) hydrostatic precompaction to close up sampling-induced microcracks, (2) applying deviatoric stresses to determine damage and permeability changes, and (3) recompression along different loading paths to examine reversibility of the damage. The critical stress conditions at the onset of dilatancy, permeability percolation, failure strength, and residual strength are determined. An empirical model is established for fracturing-induced permeability by considering the effects of connectivity and conductivity of microcracks. The cubic law is validated for the variation of permeability of connected fractures with closure. The experiments and results are also presented and discussed.

1. Introduction

Excavation of underground openings leads to a redistribution of the rock stress, particularly to a high concentration of deviatoric stresses in the surrounding rock where radial stresses are decreased. This results in fractures and permeability increase in the near-field if the damage and failure criteria of the rock are violated. As observed in the Underground Research Laboratories (URLs) at Mont Terri in Switzerland (Bossart et al., 2004; Blümling et al., 2007) and at Bure in France (Armand et al., 2014), the excavation damaged zone (EDZ) in the Opalinus and Callovo-Oxfordian argillaceous formations is developed near drift walls and the permeability increases over several orders of magnitude. However, reconsolidation of the EDZ can be expected due to convergent compression of the surrounding clay rock, the increasing resistance of the backfill/seal materials, and additionally the water-induced swelling of clay minerals into fracture interstices. For reliable predictions of the EDZ development and for an assessment of its impact on the long-term safety of a radioactive waste repository, it is necessary to establish a robust database and adequate constitutive models for description of the hydromechanical behaviour of the host rock.

During the last decade, the hydromechanical behaviour of the Callovo-Oxfordian and Opalinus clay rocks, which are being investigated as the potential host rocks for radioactive waste repositories (Nagra, 2002; Andra, 2005), has been extensively studied in laboratory experiments. Most of the investigations focused on the stress–strain–permeability behaviour of the clay rocks during the pre-failure phase (Renner et al., 2000; Zhang and Rothfuchs, 2004, 2008; Corkum and Martin, 2007; Naumann et al., 2007; Popp and Salzer, 2007; Jobmann et al., 2010; Amann et al., 2014). The knowledge of the pre-failure behaviour is useful for the evaluation of the intensity and extent of the EDZ as well as for an adequate design of the support measures for the openings. More important is, however, the post-failure behaviour of the damaged host rock for prediction of the reconsolidation process of the EDZ during the long-term post-closure phase of the repository. This important issue has been not yet intensively investigated and so far there are only very limited data available (Davy et al., 2007; Bock et al., 2010; Zhang, 2013, 2015). In order to characterise the complete pre- and post-failure behaviours of clay rock, a new series of laboratory experiments has been performed on the Callovo-Oxfordian claystone. The experiments and results are also presented and discussed in this paper.

2. Preparation and characterisation of samples

Core samples were extracted from the Callovo-Oxfordian argillaceous formation at the −490 m main level of the Meuse/Haute-

* Corresponding author. Tel.: +49 5318012219.
E-mail address: chun-liang.zhang@grs.de.

Peer review under responsibility of Institute of Rock and Soil Mechanics, Chinese Academy of Sciences.
1674-7755
http://dx.doi.org/10.1016/j.jrmge.2015.10.001

Marne URL (MHM-URL) in France. The boreholes were drilled horizontally parallel to the bedding planes. In order to prevent desaturation and damage, the drilled cores were confined in special cells developed by Andra (2005) and stored in a climate-controlled room at 22 °C before testing. Cylindrical samples were carefully prepared from the cores to a size of 70 mm diameter and 140 mm length by cutting and smoothing the surfaces in a lathe. Because of the high sensitivity of the clay rock to changes of the environment, microcracks were unavoidably induced by sampling. They mostly oriented along the bedding planes.

The samples were characterised by measurement of their mineralogical composition and physical properties. On average, the claystone at the sampling locations contains 27–42% clay minerals, 28–38% carbonates, 26–36% quartz and small amounts of other minerals (Andra, 2005). The physical properties obtained from more than 30 samples are: grain density = (2.7 ± 0.01) g/cm^3, bulk density = (2.4 ± 0.02) g/cm^3, porosity = (16.8 ± 1)%, water content = (6.5 ± 0.8)%, and degree of water saturation = (90 ± 6)%. It has to be pointed out here that the disturbed samples are not quite representative for the intact natural rock that is water-saturated and highly-consolidated under the geologically confined conditions. For gathering more representative data for the intact rock, the quality of the samples has to be improved. This was done by hydrostatically compressing the samples up to the in situ rock stress and even higher stresses.

3. Testing method and procedure

Triaxial compression tests were carried out on the samples to measure various mechanical and hydraulic parameters. Fig. 1 illustrates schematically the test principle. The sample is inserted in a rubber jacket and covered between two load pistons, in which piezo-electric wave transducers are installed for ultrasonic wave measurement to detect changes in the inner structure of the sample. Axial strain ε_1 is monitored using a linear variable differential transducer (LVDT) installed outside the cell, while radial strain ε_3 is recorded using a circumferential extensometer chain mounted around the sample. Based on the measured axial and radial strains, the volumetric strain can be obtained by $\varepsilon_v = \varepsilon_1 + 2\varepsilon_3$. The hydraulic system allows monitoring fluid flow through the sample in the axial direction. In the tests, nitrogen gas was injected at the bottom at a constant pressure of 0.2 MPa and the outflow was determined by feeding the gas at the top into a burette at atmospheric pressure. To ensure gas flow through the generated fractures in case they did not link the end faces of the sample directly, two thin filter sheets were inserted between sample and jacket in the upper and lower sections along about 1/6 of the sample length each, which was estimated assuming a fracture inclination angle of about 30° to the major principal stress σ_1. From the steady-state gas flow, the apparent gas permeability is obtained according to Darcy's law for compressive media:

$$k = 2\mu \frac{p_o q}{p_i^2 - p_o^2} \frac{l}{A} \quad (1)$$

where k is the gas permeability (m^2), q is the flow rate of the gas (m^3/s), μ is the dynamic viscosity of the gas (Pa s), l is the effective length of the sample (m), A is the cross section of the sample (m^2), p_i is the inlet pressure (Pa), and p_o is the outlet pressure (Pa).

The tests were divided into two groups comprising at least 10 samples each for examining the repeatability of the results. Table 1 gives the test conditions and major results. A common test procedure was carried out for three sequential loading stages:

(1) Hydrostatic precompaction up to 15 MPa (group I) and 20 MPa (group II) to improve the quality of the samples, which are equivalent to and even higher than the in situ lithostatic stresses of 12.5–16 MPa at the sampling positions (Armand et al., 2014);
(2) Deviatoric loading by axial compression at a rate of 10^{-6} s^{-1} and at a lateral confining stress increasing from 0.5 MPa up to 12 MPa to investigate the deviatoric stress–strain response, damage and permeability changes of the intact claystone; and
(3) Recompression along different loading paths that are expected in the EDZ to examine the post-failure behaviour of the fractured claystone.

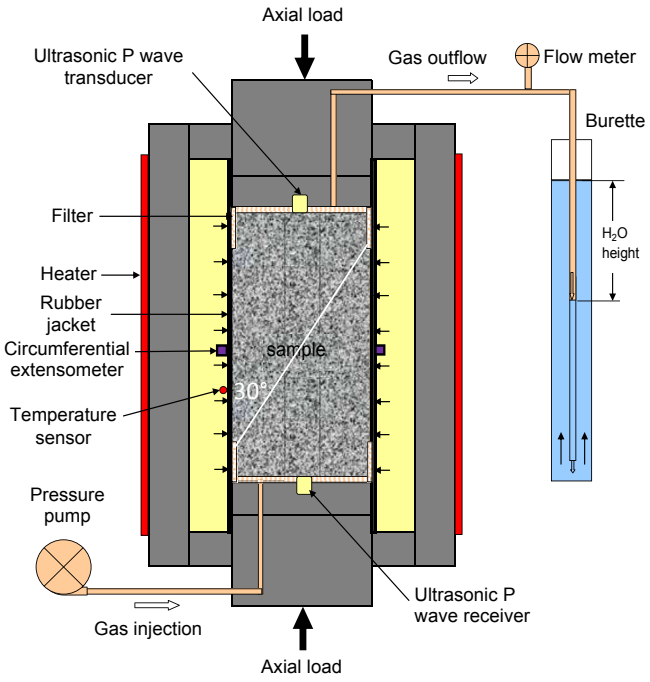

Fig. 1. Schematic assembly of a sample in triaxial cell with measurements of deformation, gas permeability, and ultrasonic wave velocity.

4. Test results and interpretation

4.1. Hydrostatic precompaction

Some typical results of the precompaction up to 20 MPa are presented in Fig. 2 in terms of volumetric strain and gas permeability versus applied hydrostatic load and unload. The stress–strain (σ_m–ε_v) curves along loading path show that the volumetric compaction is nonlinearly related to the hydrostatic load in the initial stage and then follows a linear relation. The initial nonlinear compaction is mostly attributed to the closure of the sampling-induced microcracks that are mostly aligned with the bedding planes in the axial direction. This becomes apparent by comparing the local strains perpendicular ($\varepsilon_\perp$) and parallel ($\varepsilon_{//}$) to the bedding planes, as shown in Fig. 3. The strain $\varepsilon_\perp$ is larger than $\varepsilon_{//}$ indicating less resistance to compaction in the normal direction of the cracks. The subsequent linear compaction is due to the elastic closure of the cracks and the pores in the matrix. Additionally, the progressive compaction at constant load indicates the viscoplastic deformation of the inner pore structure.

Table 1
Triaxial test conditions and characteristic parameters for the stress–strain–permeability behaviour of the samples.

Test		Lateral stress, σ_3 (MPa)	Yield stress, σ_Y (MPa)	Dilatancy threshold and strain		Peak strength and strain		Percolation threshold and strain		Gas permeabilities		Stress ratios		Fracture angle, β (°)
				σ_D (MPa)	ε_D (%)	σ_B (MPa)	ε_B (%)	σ_P (MPa)	ε_P (%)	k_o (m^2)	k_f (m^2)	σ_Y/σ_B	σ_D/σ_B	
Group I	1	1	11.6	14.2		18.5		15.3<	0.04	9×10^{-21}	3×10^{-15}	0.63	0.77	25
	2	2	13.8	23	0.07	23.5	0.07	21.3>	0.04	2×10^{-20}	2×10^{-19}	0.59	0.98	30
	3	2.5	16	23	0.29	24	0.28	14.2>	0.25	5×10^{-18}	2×10^{-16}	0.67	0.96	30
	4	3	17.2	25	0.39	26.6	0.39	24.6>	0.38	1×10^{-16}	3×10^{-15}	0.65	0.94	25
	5	4	12.7	19.5		23		18.5>	0.13	9×10^{-21}	1×10^{-16}	0.55	0.85	27
	6	5	16.9	25	0.48	25.4	0.48	15.7>	0.46	8×10^{-21}	1×10^{-19}	0.67	0.98	25
	7	6	16.5	27.5		30.9				2×10^{-20}	1×10^{-20}	0.53	0.89	35
	8	8	21	35	0.25	36.4	0.25			2×10^{-17}	2×10^{-20}	0.58	0.96	25
	9	8	22.6	33	0.38	33	0.38			8×10^{-16}	8×10^{-18}	0.68	1	35
	10	10	18	30	0.41	30.7	0.4			9×10^{-19}	6×10^{-20}	0.59	0.98	32
	11	12	20.2	34	0.65	35.1	0.65			1×10^{-20}	6×10^{-21}	0.58	0.97	27
Group II	1	0.5	11	17	0.13	19.7	0.09	15.1<	0.13			0.56	0.86	23.9
	2	1	14.5	18.7	0.09	21.8	0.03	17.2<	0.08	1×10^{-16}	1×10^{-14}	0.67	0.86	25.9
	3	1	13.5	23	0.37	23.5	0.36	23<	0.37	4×10^{-21}	4×10^{-14}	0.57	0.98	19
	4	2.5	11.8	21.8	0.17	25.9	0.16	24>	0.16	3×10^{-18}	7×10^{-16}	0.46	0.84	23
	5	3	15.5	24.7	0.44	26.9	0.43	25.6>	0.41	5×10^{-21}	1×10^{-15}	0.58	0.92	22
	6	5	16.3	26.7	0.27	27.8	0.25	26.3>	0.23	1×10^{-22}	7×10^{-17}	0.59	0.96	20
	7	7	17.4	27.4	0.43	28	0.43	27.9>	0.41	9×10^{-22}	6×10^{-19}	0.62	0.98	24
	8	8	18	29.1	0.34	31	0.32	28.7>	0.33	4×10^{-22}	1×10^{-21}	0.58	0.94	30
	9	10	22	33	0.56	34.5	0.5			1×10^{-17}	8×10^{-19}	0.64	0.96	29.1
	10	10	21.9	32		33.1				1×10^{-20}	1×10^{-22}	0.66	0.97	

Note: k_o is the initial permeability; k_f is the final permeability after fracturing; <: percolation before the peak strength; >: percolation after the peak strength; mean values of σ_Y/σ_B, σ_D/σ_B and β are 0.6, 0.93 and 27°, respectively.

Depending on the intensity of the disturbances in the samples, the maximum degree of compaction reached at the applied maximum stress varies from one sample to another. The samples that had been stored for more than one year were more disturbed and thus more compacted to relatively high values of $\varepsilon_v = 1$–2.5% at a stress of 15 MPa (group I), while the compaction of the other slightly disturbed samples is lower at $\varepsilon_v = 0.3$–0.8% even at the higher stress of 20 MPa (group II). Finally, from the data for the unloading path, one can identify some reversible expansion due to the elastic reopening of the preclosed cracks and pores. The remaining compaction implies the plastic closure of the cracks.

Corresponding to the closure of the cracks, the permeability decreases significantly by several orders of magnitude from the initial values of $k_o = 10^{-13}$–10^{-19} m^2 to very low levels of $k_f = 10^{-20}$–10^{-22} m^2 at a stress of 20 MPa (Fig. 2b). The more disturbed samples (group I) showed a reduction in permeability from $k_o = 10^{-13}$–10^{-16} m^2 to $k_f = 10^{-18}$–10^{-20} m^2 at a stress of 15 MPa. The low permeabilities did not increase significantly when unloading back down to 1–3 MPa. This is attributed to the permanent closure and disconnection of the crack networks.

Even though the sampling-induced microcracks were mostly closed up by compaction, a full recovery of the original intact state could not be achieved. In fact, the intact claystone is practically impermeable for advective transport of gas under the usually encountered pressure gradients (Horseman et al., 1996; Zhang, 2015).

4.2. Deviatoric compression

The precompacted samples were deviatorically stressed at lateral stresses of 0.5–12 MPa to examine the deviatoric stress–strain–permeability behaviour of the claystone, particularly stress-driven damage evolution and permeability changes. Because the test results in both groups are well repeatable within a relatively small scatter of about 10%, only those of the second group are illustrated in Fig. 4 in terms of differential stress ($\Delta\sigma = \sigma_1 - \sigma_3$) vs. axial/radial strain (ε_1, ε_3), volumetric strain vs. axial strain (ε_v–ε_1), and permeability evolution with axial strain (k–ε_1). The short stress relaxations in some tests result from keeping the axial strain ε_1 constant during the measurements of permeability. After testing, the failure patterns of the samples were examined. Fig. 5 shows some pictures of the typical fractured samples.

4.2.1. Characterisation of the pre-failure behaviour

Fig. 6 shows a typical example of the stress–strain–permeability response of the claystone and a conceptual mode of crack evolution during triaxial loading. The establishment of this mode takes into account the micro-tomography of localised damage and deformation made on the same claystone during triaxial loading (Viggiani et al., 2011), and also the typical fracture pattern observed on the samples after testing (cf. Fig. 5). The stress–strain–permeability behaviour may be characterised in four sequential stages:

(1) The claystone deforms relatively largely in the very beginning of the load due to the closure of the remaining microcracks, and then it follows a linear axial compression ε_1, radial extension ε_3 and volumetric compaction ε_v until a deviation appears at a differential stress σ_Y. The yield point indicates the onset of microcracking, as detected by shear wave velocity on the Opalinus claystone (Popp and Salzer, 2007). The yield stress recorded is about 60% of the peak failure strength σ_B.
(2) Further increasing the stress results in a nonlinear plastic hardening process with an overall volume compaction. This implies that the pre-existing and newly created microcracks mostly keep closed during shearing (Viggiani et al., 2011). As a result, the initially very low permeability does not change much.
(3) When the deviatoric stress reaches a high value σ_D close to the peak σ_B, the volume compaction changes over to dilatation due to crack opening. Exceeding the dilatancy threshold, the microcracks grow and propagate much faster with further loading. Just as some of the neighbouring microcracks coalesce to a continuous network through the sample, the permeability begins to rise. The corresponding differential stress σ_P is usually

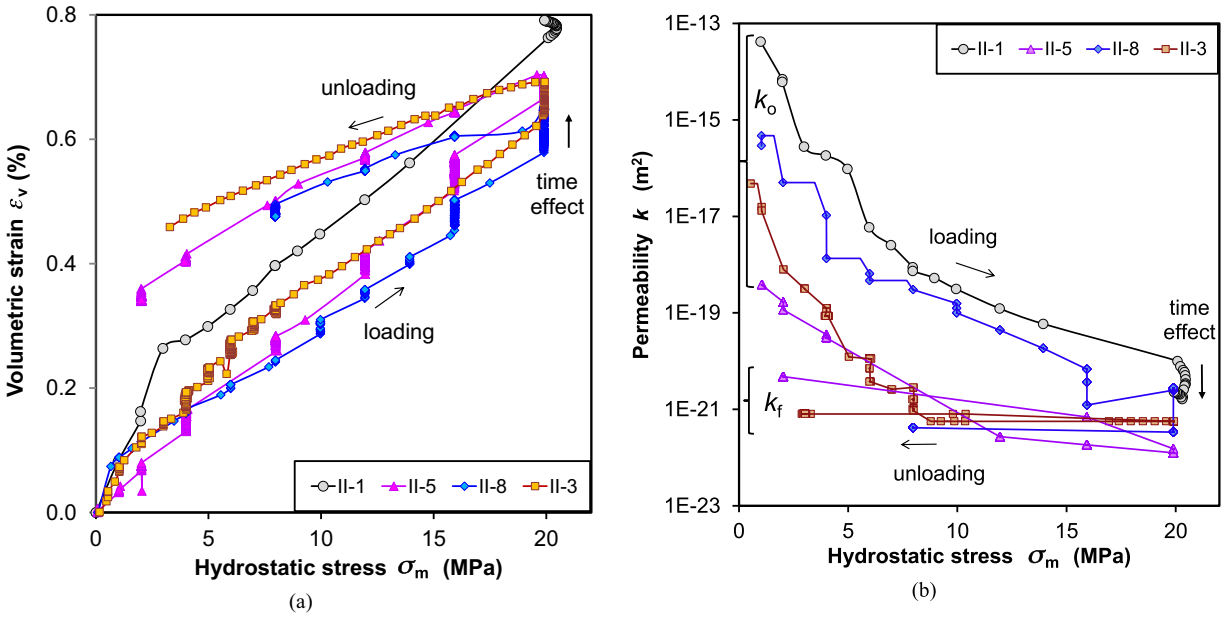

Fig. 2. Volumetric compaction (a) and permeability change (b) of claystone samples during hydrostatic loading and unloading.

called percolation threshold. It occurs shortly before the peak failure at low lateral stresses $\sigma_3 \leq 1$ MPa but shortly after the peak at high lateral stresses. So it is reasonable to assume $\sigma_P \approx \sigma_B$.

(4) Beyond the fracture percolation during the post-failure phase at the residual stress, the connection of the cracks results in a spontaneous increase of the permeability, accompanied with very small dilatancy. After the crack connectivity is sufficiently developed, further deformation is mainly dominated by fracture slipping, so that the increase of the fracturing-induced permeability is limited.

The damage and the resulting permeability change are dependent on the lateral confining stress. As the confining stress is increased, the inner structure of the claystone becomes more compacted and fracturing is inhibited. The deformation changes progressively from brittle to ductile (see Fig. 4). Because high confining stresses suppress the initiation, growth and propagation of cracks, the compaction phase before the onset of dilatancy lasts longer and the fracture percolation occurs later on at high lateral stresses. The increased permeability is also relatively low at high confining stresses. Generally, the critical stresses and strains at yield, dilatancy, percolation, and peak failure increase with increasing lateral confining stress.

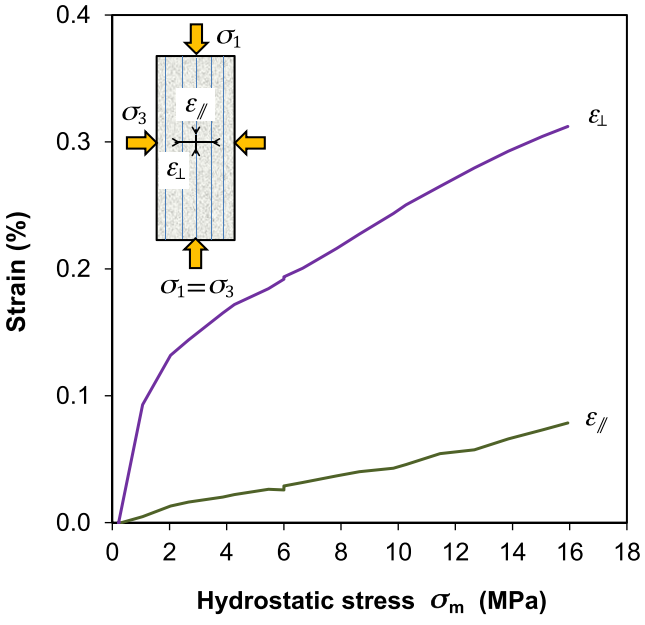

Fig. 3. Local strains perpendicular $\varepsilon_\perp$ (radial) and parallel $\varepsilon_{//}$ (axial) to the bedding planes obtained during hydrostatically compressing a claystone sample.

4.2.2. Damage and failure conditions

These critical stresses and strains identified from the stress–strain curves are summarised in Table 1 for each sample. It appears that the ratios of the yield and dilatant stresses to the peak strength are more or less constant, being independent of the confining stress. The average values are obtained as $\sigma_Y/\sigma_B = 0.6 \pm 0.05$ and $\sigma_D/\sigma_B = 0.93 \pm 0.06$. As mentioned earlier, the percolation threshold and peak failure take place almost simultaneously, i.e. $\sigma_P \approx \sigma_B$.

The critical stresses (σ_Y, σ_D, σ_P, σ_B) are plotted in Fig. 7 as functions of the lateral stress σ_3. The relationships can be described by the well-known Mohr–Coulomb and Hoek–Brown criteria. The peak strength data are fitted by the following envelopes.

(1) For Mohr–Coulomb criterion, we have

$$\sigma_B = \sigma_{1B} - \sigma_3 = 2c\tan\left(45^\circ + \frac{\varphi}{2}\right) - \sigma_3\left[1 - \tan^2\left(45^\circ + \frac{\varphi}{2}\right)\right] \quad (2)$$

where σ_{1B} is the axial peak failure stress; c and φ are the cohesion and the internal friction angle, respectively, and $c = 6.5$ MPa and $\varphi = 24^\circ$.

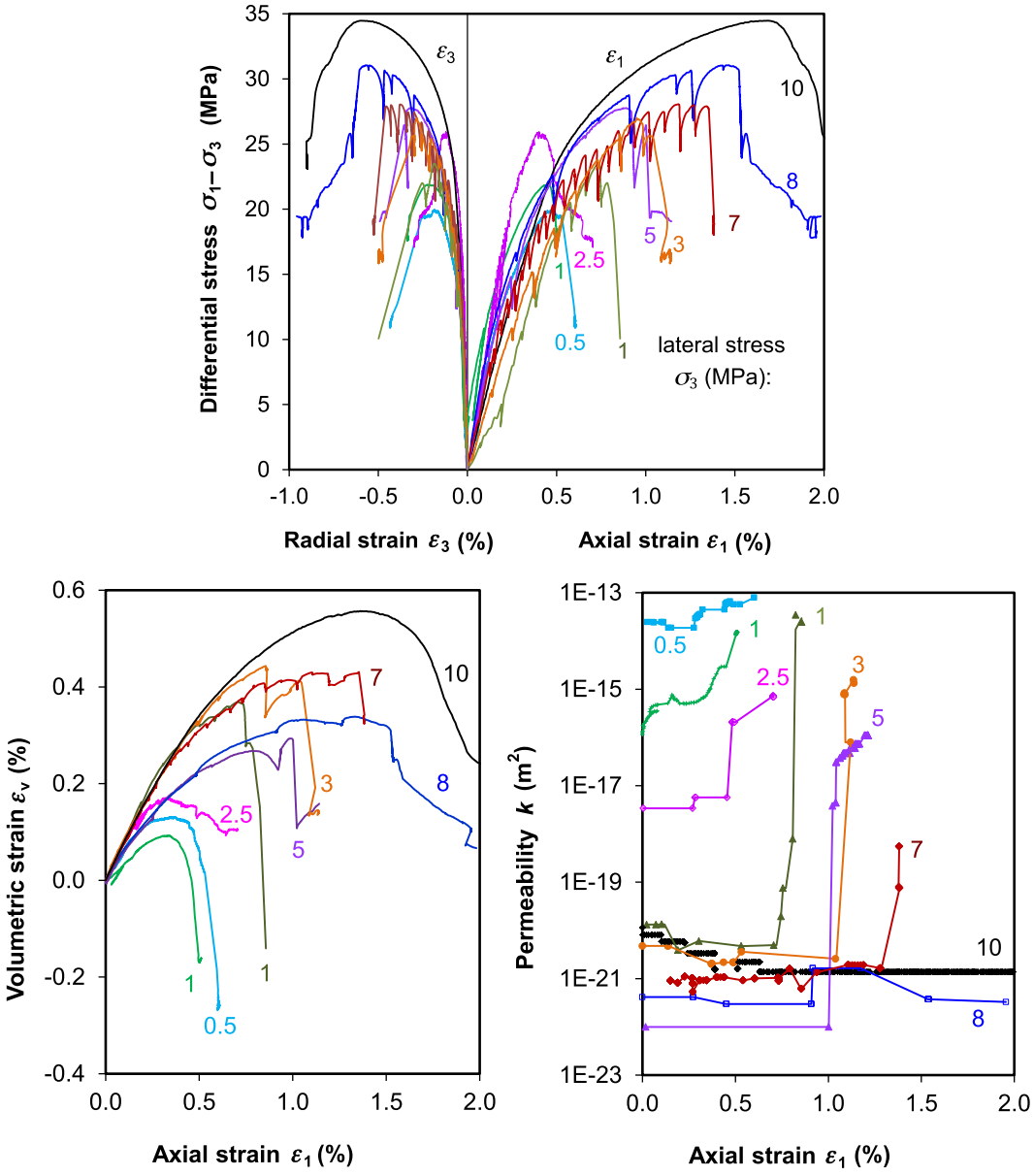

Fig. 4. Deviatoric stress–strain–permeability curves obtained on the precompacted samples at different confining stresses.

(2) For Hoek–Brown criterion, we have

$$\sigma_B = \sigma_{1B} - \sigma_3 = \left(m\sigma_c\sigma_3 + s\sigma_c^2\right)^{1/2} \quad (3)$$

where σ_c is the uniaxial compressive strength which is determined to be 19 MPa, and the other parameters $m = 4$ and $s = 1$.

Inserting the constant stress ratios mentioned above into Eqs. (2) and (3), respectively, obtaining the yield, dilatancy and percolation boundaries is straightforward. The Mohr–Coulomb and Hoek–Brown criteria curves are close to each other and fit the data of each critical stress (σ_Y, σ_D, $\sigma_P \approx \sigma_B$) well. These stress boundary conditions are helpful for characterising the state of the rock subjected to any given stress state. For stresses below the yield boundary σ_Y, the rock behaves elastically. Above the yield boundary but below the dilatancy boundary, $\sigma_Y < \sigma_1 - \sigma_3 < \sigma_D$, the overall volume is under compression without damage even though some microcracks are created. If the dilatancy boundary is violated, $\sigma_1 - \sigma_3 \geq \sigma_D$, the microcracks grow and coalesce with increasing deviatoric stresses. When the stress reaches the percolation and failure boundary, $\sigma_1 - \sigma_3 \geq \sigma_P \approx \sigma_B$, a crack network builds up leading to a spontaneous increase of the permeability and to failure.

Additionally, the Mohr–Coulomb criterion also predicts a shear plane angle oblique to the direction of the major principal stress σ_1, i.e. $\beta = 45° - \varphi/2 = 33°$. This value slightly overestimates the measured values of $\beta = 27° \pm 4°$. From Fig. 5 one can see that the development of cracks is localised along a single or a few major shear planes, which are crossing the bedding planes at angle of $90°-\beta \approx 63° \pm 4°$. This indicates that shearing the claystone matrix is the typical failure mode under triaxial compression conditions.

4.2.3. Permeability induced by fracturing

The fracturing-induced permeability observed in the tests (Fig. 4) is represented in Fig. 8 as a function of the related volumetric strain and the applied lateral stress. The data show that (a) the initial permeability of each sample does not change much until

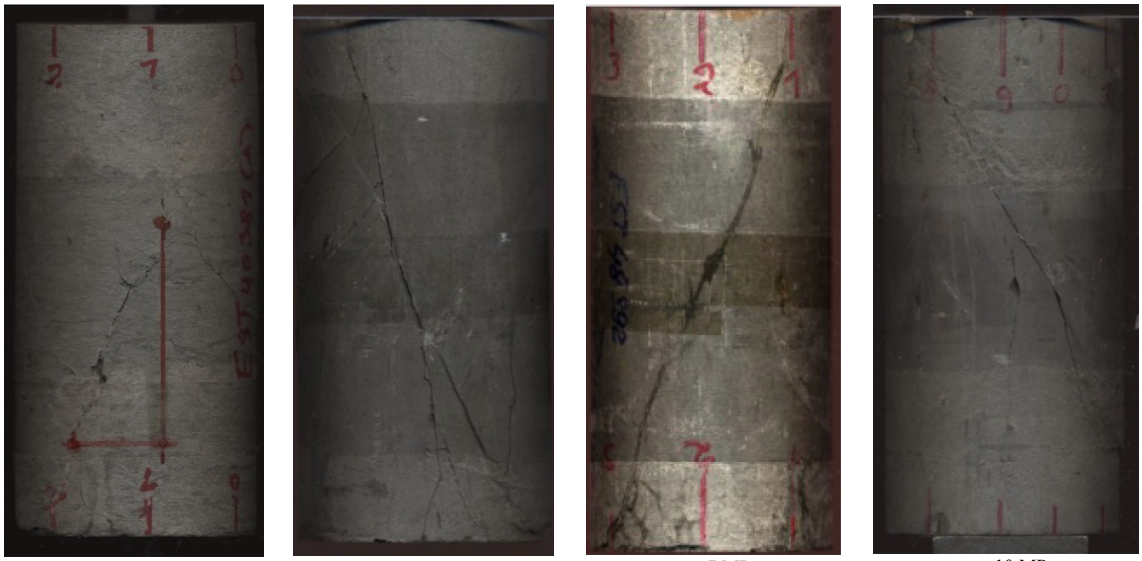

Fig. 5. Typical patterns of fractures observed on the samples after failure at different confining stresses.

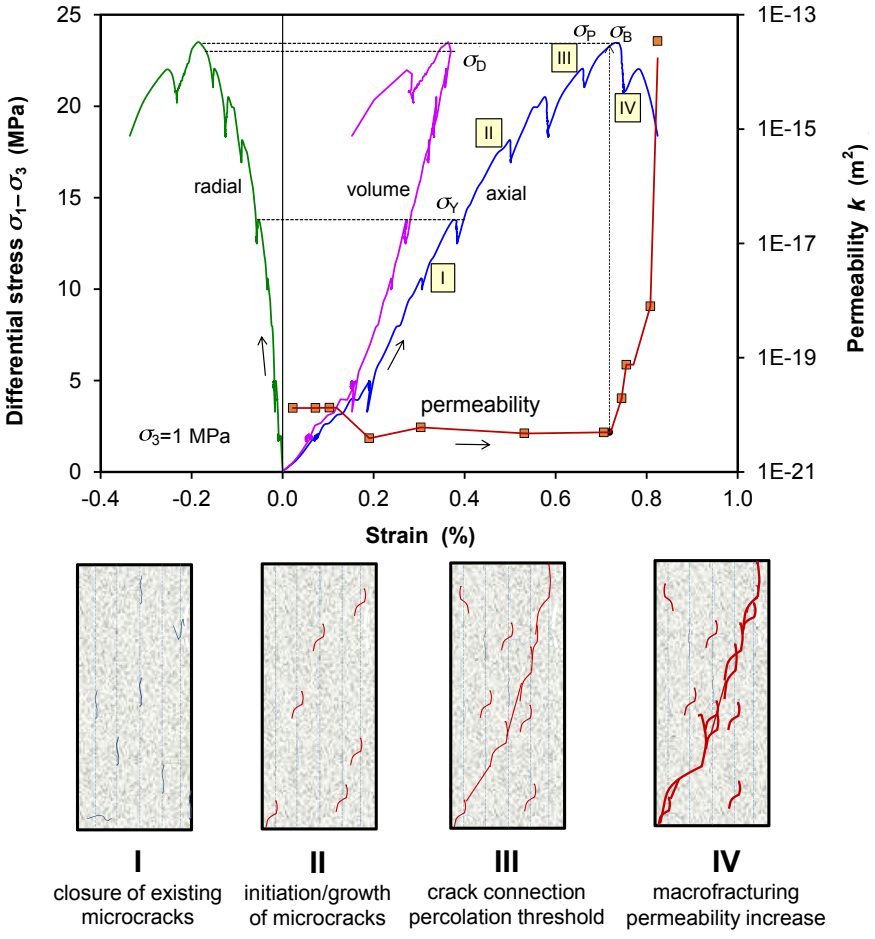

Fig. 6. Stress–strain–permeability behaviour of the claystone including thresholds of yield σ_Y, dilatancy σ_D, percolation σ_P, and peak failure σ_B.

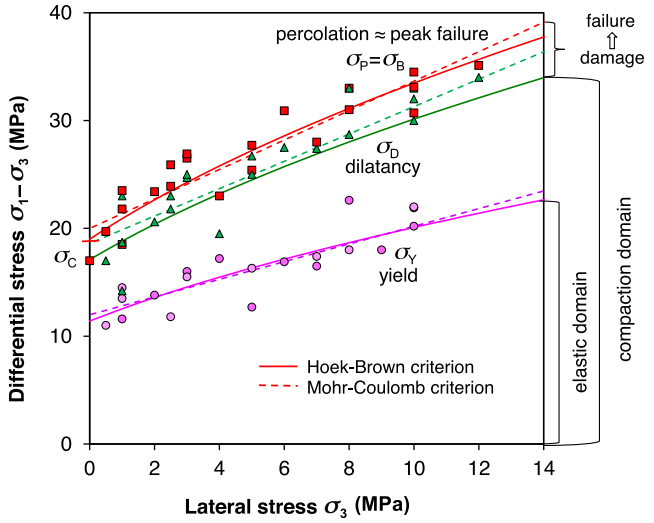

Fig. 7. Stress boundaries of yield, dilatancy, percolation and peak failure of the claystone.

percolation begins at the volume compaction ε_P; (b) the subsequent sudden increase in permeability is accompanied by small dilatancy of less than 0.1%; (c) the smaller the lateral stress is, the higher the sudden permeability increase is; and (d) the reached high permeability varies very slightly with further dilatancy. The final permeabilities after sufficient fracturing range from $k_f = 10^{-13}$ m^2 at $\sigma_3 = 0.5$ MPa to $k_f = 10^{-21}$ m^2 at $\sigma_3 = 8$ MPa. At higher lateral stresses $\sigma_3 \geq 8$ MPa, the permeability does not change much with dilatancy. This suggests that the cracks are highly under compression and not interconnected sufficiently to form a pathway.

The fracturing-induced permeability increase reflects the percolation behaviour due to interconnection of stress-driven cracks. Based on percolation theory, several percolation models have been developed for the fracturing-induced permeability in rocks in relation with geometry, density and distribution of microcracks (Guéguen and Dienes, 1989; Peach, 1990; Guéguen and Palciauskas, 1994; Alkan, 2009). Contributions of the connectivity and the conductivity of cracks to the apparent macroscopic

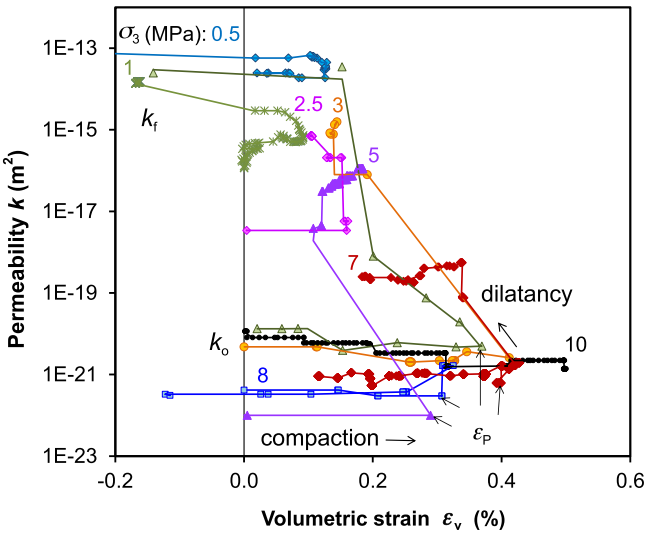

Fig. 8. Permeability evolution with volumetric strain at different lateral stresses.

permeability are considered in these models leading to a general form for fracturing-induced permeability:

$$k = k_f P \tag{4}$$

where k_f is the ultimate permeability of the fractured rock with fully interconnected cracks and P is the percolation probability defining the fraction of cracks belonging to the conductive part of a network.

The ultimate fracture permeability k_f increases with decreasing minor principal stress σ_3, as shown by the measured data in Fig. 9. The k_f–σ_3 relationship can be approximated by an exponential function:

$$k_f = k_o \exp(-\gamma\sigma_3) \tag{5}$$

where k_o is the permeability at the minor principal stress $\sigma_3 = 0$ and γ is a parameter characterising the dilatability of the interconnected cracks. The values of the parameters are estimated to be $k_o = 3 \times 10^{-13}$ m^2 and $\gamma = 1.9$ MPa^{-1}.

The percolation probability P can be expressed in terms of different variables such as crack density (Guéguen and Dienes, 1989), dilatancy (Peach, 1990), and deviatoric stress (Alkan, 2009), combined with other geometric parameters of microcracks. Because some of the crack parameters vary with loading and practically are not measurable, the application of these models is limited. Therefore, a simple model is proposed here for the percolation probability based on the measurable parameter dilatancy:

$$P = 1 - \exp\left(-\frac{\Delta\varepsilon_D}{\varepsilon_P}\right) \tag{6}$$

where $\Delta\varepsilon_D = |\varepsilon_v - \varepsilon_P|$ is the dilatancy after the percolation threshold at ε_P. Substitution of Eqs. (5) and (6) into Eq. (4) gives the final expression of fracturing-induced permeability as a function of minimum principal stress and dilatancy:

$$k = k_o \exp(-\gamma\sigma_3)\left[1 - \exp\left(-\frac{\Delta\varepsilon_D}{\varepsilon_P}\right)\right] \tag{7}$$

At $\Delta\varepsilon_D = 0$ ($\varepsilon_v = \varepsilon_P$), it follows that $P = 0$, which can be interpreted as a complete disconnection of the cracks. With increasing dilatancy, the system of cracks tends to a full connection, $P \to 1$ as $\Delta\varepsilon_D \to \infty$. In fact, a sufficiently high connectivity of the cracks for a high and final permeability can develop at very small dilatancy, for instance, $\Delta\varepsilon_D < 0.1\%$ as observed on the claystone in the tests.

The model predictions for the permeability evolution at exceeding dilatancy are compared in Fig. 10 with the data obtained during fracturing at different lateral stresses. It is evident that the fracturing-induced permeability with the spontaneous increase due to the formation of a continuous crack network and the subsequent considerable slowdown of this increase with further development of the network can be reasonably described by the model. However, more experiments are needed to confirm the parameters obtained here.

4.3. Recompression of fractured claystone

The post-failure behaviour of the damaged claystone was investigated by recompressing the pre-fractured samples along different loading paths: (a) hydrostatic compaction by simultaneously increasing axial and lateral stresses $\sigma_1 = \sigma_2 = \sigma_3$; and (b) multistep deviatoric compression by increasing σ_1 at increased lateral stress σ_{3-i} in several steps $i = 1, 2, 3, \ldots, n$.

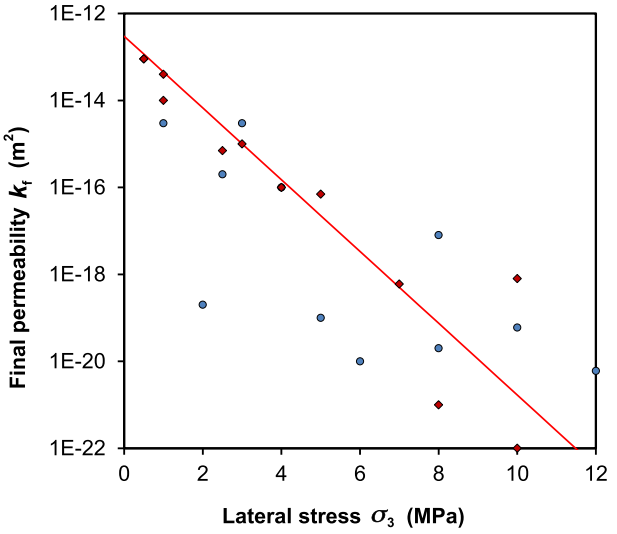

Fig. 9. Final permeabilities reached after fracturing as a function of lateral stress.

4.3.1. Hydrostatic recompaction

Fig. 11 shows the results of two hydrostatic recompaction tests on the fractured samples (Nos. 3 and 7 in group II) in terms of volumetric strain and permeability as a function of the applied load. It can be seen that (a) the increase of hydrostatic stress closes up the fractures and hence decreases the fracture permeability; and (b) the subsequent unloading leads to some elastic reopening of the fractures without significant reversibility of the permeability. It suggests that parts of the fractures have been permanently closed and disconnected from the pathway. The compaction–permeability relation obtained on the stressing-fractured samples is quite similar to that of the sampling-disturbed samples (cf. Fig. 2). The quantitative differences are caused by different features of the fractures such as the size, geometry, roughness, and connectivity.

4.3.2. Multistep deviatoric recompression

Supplementary to the hydrostatic recompaction, most fractured samples were deviatorically reloaded step by step. The multistep loading procedure began with a low lateral stress, at which the axial stress was increased to achieve a sufficiently large deformation and then unloaded shortly. This procedure was repeated several times at increased lateral stresses up to 10–20 MPa. Typical results are illustrated in Fig. 12 for three samples with different initial lateral stresses in terms of differential stress vs. axial and radial strains ($\Delta\sigma$–ε_1 and $\Delta\sigma$–ε_3), and volumetric strain and permeability vs. axial strain (ε_v–ε_1 and k–ε_1).

The stress–strain curves show that (a) the post-failure behaviour at each elevated lateral stress is quite similar to the behaviour under pre-failure conditions, i.e. nonlinear axial compression, radial extension and volume compaction until the onset of dilatancy at σ_D; (b) the stress does not increase much with strain because further deformation is dominated by plastic sliding of the fractures; (c) the maintaining dilatancy stress σ_D represents the maximum residual stress-bearing capacity σ_R of the fractured claystone; and (d) the residual strength increases with increasing lateral stress σ_3.

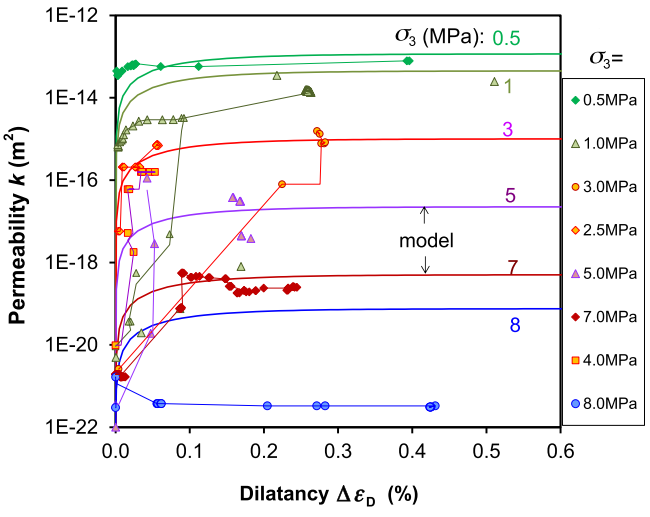

Fig. 10. Prediction of the fracturing-induced permeability in the claystone using the newly formulated percolation model.

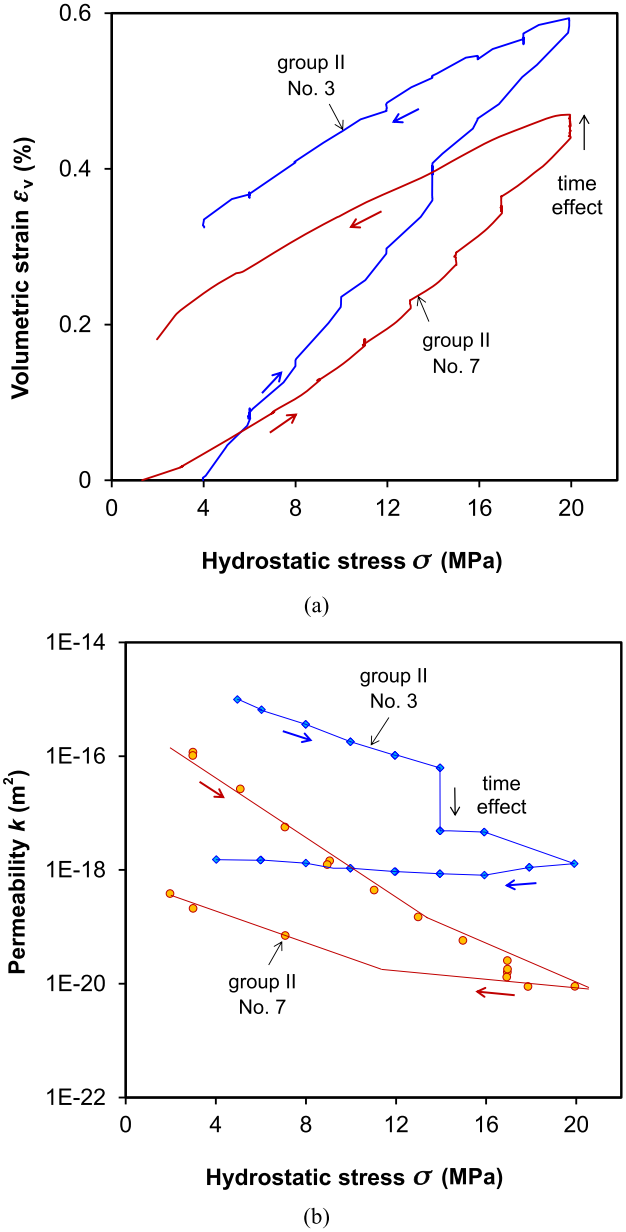

Fig. 11. Volume recompaction (a) and permeability change (b) of the fractured samples during hydrostatic loading and unloading.

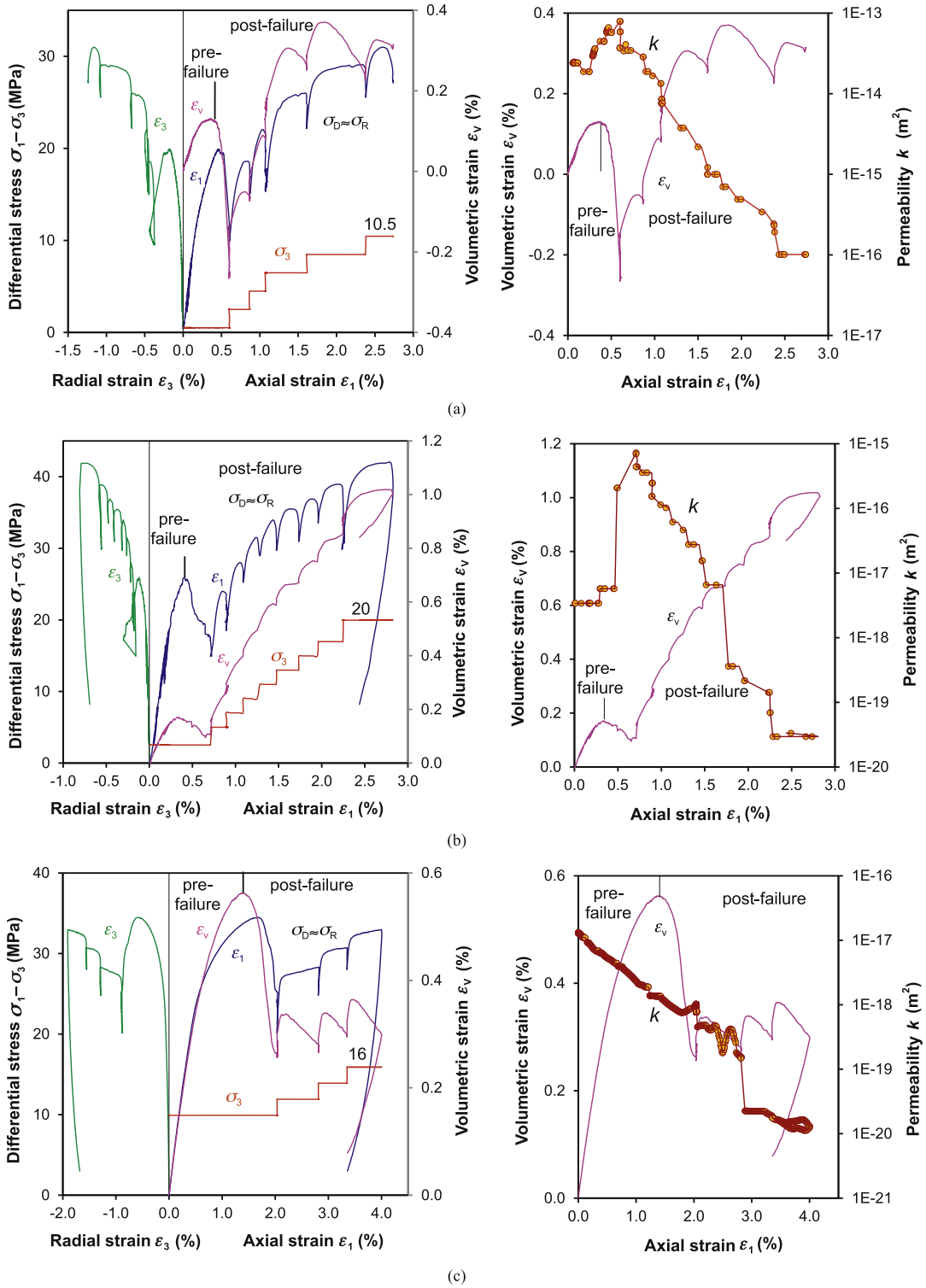

Fig. 12. Stress–strain–permeability behaviour of fractured claystone during multistep deviatoric loading. (a) Lateral stress σ_3 = 0.5 → 10.5 MPa. (b) Lateral stress σ_3 = 2.5 → 20 MPa. (c) Lateral stress σ_3 = 10 → 16 MPa.

The residual strengths obtained on the samples (EST34713B, etc.) at different lateral stresses are depicted in Fig. 13. For each individual sample, the residual strength is nonlinearly related to the minor principal stress. This can reasonably be described by the Hoek–Brown criterion (Eq. (3)). However, the residual strength varies from a sample to another due to different damage intensities produced during the pre-failure stage. The relatively large bandwidth of the residual strength of the damaged claystone can be defined with the upper and lower boundaries with the obtained respective parameters: σ_c = 11 MPa and m = 9 for the upper boundary; σ_c = 7 MPa and m = 5 for the lower one; σ_c = 9 MPa and m = 7 for the mean curve; and s = 0 for all of them. The lower

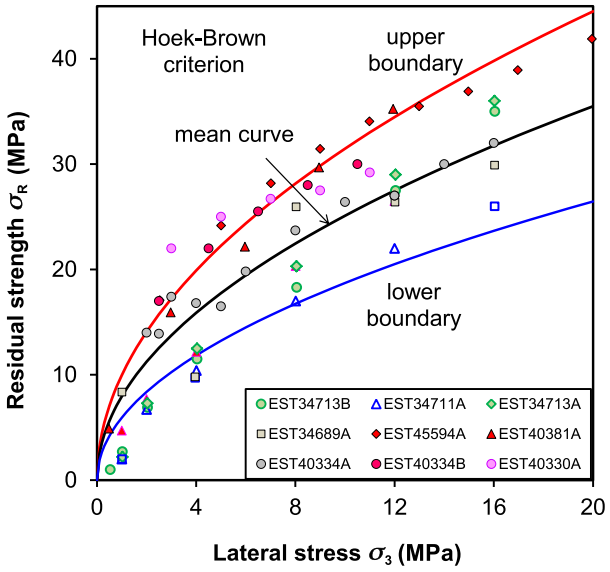

Fig. 13. Residual strength of fractured claystone as a function of minor principal stress.

boundary shall be applied for the residual strength of the heavily damaged clay rock near drift walls, while the upper one for the less damaged rock mass in the far-field.

4.3.3. Permeability variation with fracture closure

In correspondence with the closure of fractures or the volume compaction of the damaged claystone before the onset of dilatancy at each increased lateral stress, the permeability decreases. Further deviatoric loading gives a rise in dilatancy but the permeability does not change much. Generally, the permeability in fractured claystone is largely determined by the amplitude and distribution of the apertures and surface roughness of the interconnected fractures along the flow path. Previous investigations on the same claystone (Zhang, 2013, 2015) have shown that the relation between permeability and fracture aperture can be approximated by the cubic law developed for fluid flow through a set of parallel plates. It can be written in terms of permeability k as a function of volumetric strain ε_v:

$$k = D(\Delta\varepsilon_R)^3 = D|\varepsilon_F - \varepsilon_v|^3 \quad (8)$$

where ε_F is the maximum dilatancy reached after sufficient fracturing, $\Delta\varepsilon_R = |\varepsilon_F - \varepsilon_v|$ represents the residual voids in the fractures, and D is a parameter characterising the rock state after fracturing, $D = k_f/\varepsilon_F^3$. As the residual fracture void tends to zero, $\Delta\varepsilon_R \to 0$, the fracture permeability disappears.

Fig. 14 shows a comparison of the predicted permeability based on the cubic law and the measured permeability as a function of the residual volumetric strain during the hydrostatic and multistep deviatoric compressions. The parameter D is derived from the measured ε_F and k_f data to lie in the range of 7×10^{-10} m^2 to 1×10^{-7} m^2. A satisfactory agreement between the model and the data can be stated for the compaction phases during the deviatoric loading. However, there remain also some quantitative differences. Obviously, more experiments are needed to confirm the data and to validate the model for low fracture voids of $\varepsilon_R < 0.1\%$ and low permeabilities of $k < 10^{-17}$ m^2, where an increasing degree of disconnection of the fracture network and thus a rapid decrease in permeability are expected.

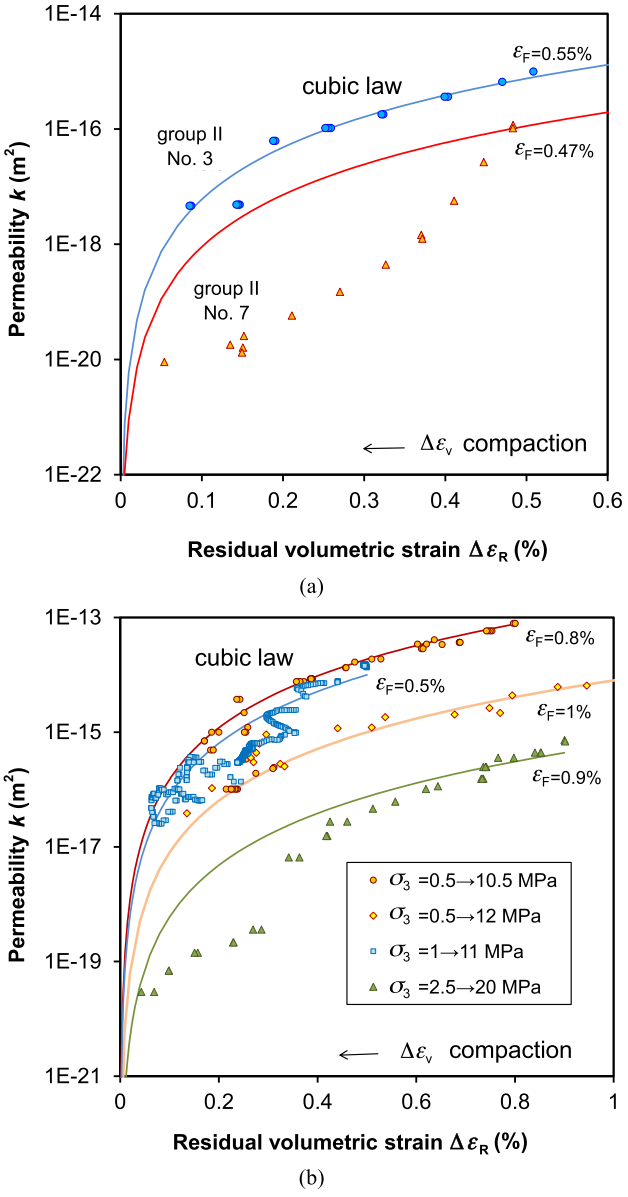

Fig. 14. Variation in permeability of fractured claystone with volume compaction during (a) hydrostatic and (b) multistep deviatoric loading.

5. Conclusions

The complete pre- and post-failure stress–strain–permeability behaviour of the Callovo-Oxfordian claystone was experimentally investigated with measurements of deformation and gas permeability during damaging and recompressing the samples. The claystone behaves elastoplastically with an overall volume compaction until the onset of dilatancy at a high stress. Closely as the peak stress is reached, a single or a few shear fractures is created leading to a spontaneous increase in permeability and to failure. The damage and failure are suppressed under high values of the minor confining stress. After failure, the claystone still possesses a certain residual strength depending on the damage intensity and the minor confining stress. When the minor principal stress is increased again, the fractures tend to be closed.

The permeability variations of the claystone with damage and recompaction can be approximated by an empirical model:

$$k = \begin{cases} k_c & (\sigma_1 - \sigma_3 < \sigma_B) \\ k_0 \exp(-\gamma\sigma_3)[1 - \exp(-\Delta\varepsilon_D/\varepsilon_P)] & (\sigma_B \geq \sigma_1 - \sigma_3 \geq \sigma_R) \\ D(\Delta\varepsilon_R)^3 & (\sigma_1 - \sigma_3 < \sigma_R) \end{cases} \quad (9)$$

The permeability of the intact claystone is very low, $<10^{-21}$ m^2, and varies negligibly until the percolation occurs at the peak stress σ_B. Beyond the peak during the post-failure phase, the fracturing-induced permeability increases exponentially with increasing dilatancy $\Delta\varepsilon_D$ and decreasing minor principal stress σ_3. When σ_3 increases again, the fractures tend to be closed and the fracture permeability reduces following the cubic law.

Conflict of interest

The author wishes to confirm that there are no known conflicts of interest associated with this publication and there has been no significant financial support for this work that could have influenced its outcome.

Acknowledgements

The present work was co-funded by the German Federal Ministry of Economics and Technology (BMWi) under contract number 02E10377 and by the European Commission (EC) as the part of the Euratom's Seventh Framework Programme FP7/2007-2013 under grant agreement No. 323273 for the DOPAS project. The support from Andra for providing the test material and for the fruitful discussions is also gratefully acknowledged.

References

Alkan H. Percolation model for dilatancy-induced permeability of the excavation damage zone in rock salt. International Journal of Rock Mechanics and Mining Sciences 2009;46(4):716–24.

Amann F, Ündül Ö, Kaiser PK. Crack initiation and crack propagation in heterogeneous sulfate-rich clay rocks. Rock Mechanics and Rock Engineering 2014;47:1849–65.

Andra Dossier. Synthesis – evaluation of the feasibility of a geological repository in an argillaceous formation. 2005. https://www.andra.fr/download/andra-international-en/document/266va.pdf.

Armand G, Leveau F, Nussbaum C, de La Vaissiere R, Noiret A, Jaeggi D, Landrein P, Righini C. Geometry and properties of the excavation-induced fractures at the Meuse/Haute-Marne URL drifts. Rock Mechanics and Rock Engineering 2014;47(1):21–41.

Bock H, Dehandschutter B, Martin CD, Mazurek M, de Haller A, Skoczylas F, Davy C. Self-sealing of fractures in argillaceous formations in the context of geological disposal of radioactive waste – review and synthesis. NEA Report No. 6184. OECD; 2010.

Bossart P, Trick T, Meier PM, Mayor JC. Structural and hydrogeological characterisation of the excavation-disturbed zone in the Opalinus clay (Mont Terri Project, Switzerland). Applied Clay Science 2004;26(1–4):429–48.

Blümling P, Bernier F, Lebon P, Martin CD. The excavation damaged zone in clay formations: time-dependent behaviour and influence on performance assessment. Physics and Chemistry of the Earth 2007;32:588–99.

Corkum AG, Martin CD. The mechanical behaviour of weak mudstone (Opalinus clay) at low stresses. International Journal of Rock Mechanics and Mining Sciences 2007;44(2):196–209.

Davy CA, Skoczylas F, Barnichon FD, Lebon P. Permeability of macro-cracked argillite under confinement: gas and water testing. Physics and Chemistry of the Earth 2007;32(8–14):667–80.

Guéguen Y, Dienes J. Transport properties of rocks from statistics and percolation. Mathematical Geology 1989;21(1):1–13.

Guéguen Y, Palciauskas V. Introduction to the physics of rocks. Princeton, USA: Princeton University Press; 1994.

Horseman ST, Higgo JJW, Alexander J, Harrington JF. Water, gas and solute movement through argillaceous media. NEA Report CC-96/1. OECD; 1996.

Jobmann M, Wilksnack TH, Voigt HD. Investigation of damage-induced permeability of Opalinus clay. International Journal of Rock Mechanics and Mining Sciences 2010;47(2):279–85.

Nagra. Project Opalinus clay: models, codes and data for safety assessment – demonstration of disposal feasibility for spent fuel, vitrified high-level waste and long-lived intermediate-level waste. Technical Report 02–06. 2002.

Naumann M, Hunsche U, Schulze O. Experimental investigations on anisotropy in dilatancy, failure and creep of Opalinus clay. Physics and Chemistry of the Earth 2007;32(8–14):889–95.

Peach CJ. Influence of deformation on the fluid transport properties of rock salts. PhD dissertation. Utrecht, the Netherlands: Instituut voor Aardwetenschappen der Rijksuniversiteit Utrecht; 1990.

Popp T, Salzer K. Anisotropy of seismic and mechanical properties of Opalinus clay during triaxial deformation in a multi-anvil apparatus. Physics and Chemistry of the Earth 2007;32(8–14):879–88.

Renner J, Hettkamp T, Rummel F. Rock mechanical characterization of an argillaceous host rock of a potential radioactive waste repository. Rock Mechanics and Rock Engineering 2000;33(3):153–78.

Viggiani G, Bésuelle P, Desrues J. X-ray micro tomography as a tool for studying localized damage/deformation in clay rock. In: NEA Clay Club Workshop Proceedings – Clay Characterisation from Nanoscopic to Microscopic Resolution, Karlsruhe, Germany; 2011.

Zhang CL, Rothfuchs T. Experimental study of the hydro-mechanical behaviour of the Callovo-Oxfordian argillite. Applied Clay Science 2004;26(1–4):325–36.

Zhang CL, Rothfuchs T. Damage and sealing of clay rocks detected by measurements of gas permeability. Physics and Chemistry of the Earth 2008;33(Supp. 1):363–73.

Zhang CL. Sealing of fractures in claystone. Journal of Rock Mechanics and Geotechnical Engineering 2013;5(3):214–20.

Zhang CL. Investigation of gas migration in damaged and resealed claystone. In: Geological Society Special Publication 415 – Gas Generation and Migration in Deep Geological Radioactive Waste Repositories. The Geological Society of London; 2015. p. 75–93.

Chun-Liang Zhang obtained his BSc and MSc degrees in Mining Engineering from Liaoning Technical University, China, in 1982 and 1984, respectively, and his PhD in Mining Engineering from Technical University of Clausthal, Germany, in 1990. He was affiliated as scientific staff with German National Research Center for Environment and Health (GSF) from 1990 to 1993, German Federal Institute for Geosciences and Natural Resources (BGR) from 1993 to 1998, Underground Research Laboratory Asse Mine from 1998 to 2001, and Repository Safety Research Division of the Gesellschaft fuer Anlagen- und Reaktorsicherheit (GRS) - Germany's leading expert organization in the nuclear safety field, since 2001. His research interests include (1) experimental investigations on the thermo–hydro–mechanical (THM) behaviours of host rocks (clay, salt, granite) and engineered barrier materials (clay-based mineral mixtures, crushed salt, etc.) for deep geological disposal of nuclear waste; and (2) theoretical study and numerical modelling of coupled THM processes in the natural-engineered barrier systems in repositories. He has been participated in a large number of European and German national projects, for instance: (1) BAMBUS: Backfilling and sealing of underground repositories for radioactive waste in salt (2000–2003); (2) MODEX-REP: Development and validation of constitutive models describing the coupled hydro-mechanical processes in the Callovo-Oxfordian clay rock during shaft sinking (2000–2002); (3) HE-D: Heating experiment in the Mont Terri Rock Laboratory to investigate THM processes in clay formations (2003–2006); (4) NF-PRO: Response of clay rocks to moisture change and self-sealing of fractures in clays (2004–2007); (5) ESDRED-SB: Self-sealing barriers of clay/mineral mixtures in a clay repository (2004–2011); (6) TIMODAZ: Thermal impact on development of excavation damaged zones in repositories in clay formations (2005–2010); (7) THERESA: Coupled thermal–hydrological–mechanical-chemical processes in repository safety assessment (2007–2009); (8) THM-TON: Thermo–hydro–mechanical behaviours of clay rocks and clay-based barrier materials (2007–2016); (9) DOPAS: Full-scale demonstration of plugs and seals (2012–2016).